Partial Accretion in the Propeller Stage of Low-mass X-Ray Binary Aql X–1

C. Güngör[1,2], K. Y. Ekşi[1] , E. Göğüş[2] , and T. Güver[3]

[1] İstanbul Technical University, Faculty of Science and Letters, Physics Engineering Department, 34469, İstanbul, Turkey; gungorcan@itu.edu.tr
[2] Sabancı University, Faculty of Engineering and Natural Science, Orhanlı—Tuzla, 34956, İstanbul, Turkey
[3] İstanbul University, Science Faculty, Department of Astronomy and Space Sciences, Beyazıt, 34119, İstanbul, Turkey

Abstract

Aql X–1 is one of the most prolific low-mass X-ray binary transients (LMXBTs) showing outbursts almost annually. We present the results of our spectral analyses of *Rossi X-Ray Timing Explorer*/proportional counter-array observations of the 2000 and 2011 outbursts. We investigate the spectral changes related to the changing disk-magnetosphere interaction modes of Aql X–1. The X-ray light curves of the outbursts of LMXBTs typically show phases of fast rise and exponential decay. The decay phase shows a "knee" where the flux goes from the slow-decay to the rapid-decay stage. We assume that the rapid decay corresponds to a weak propeller stage at which a fraction of the inflowing matter in the disk accretes onto the star. We introduce a novel method for inferring, from the light curve, the fraction of the inflowing matter in the disk that accretes onto the neutron star depending on the fastness parameter. We determine the fastness parameter range within which the transition from the accretion to the partial propeller stage is realized. This fastness parameter range is a measure of the scale height of the disk in units of the inner disk radius. We applied the method to a sample of outbursts of Aql X–1 with different maximum flux and duration times. We show that different outbursts with different maximum luminosity and duration follow a similar path in the parameter space of accreted/inflowing mass flux fraction versus fastness parameter.

Key words: accretion, accretion disks – stars: neutron – X-rays: binaries – X-rays: individual (Aql X-1)

1. Introduction

Low-mass X-ray binaries (LMXBs) are systems containing an accreting compact object—a neutron star (NS) or a black hole (BH)—and a low-mass companion ($M_c \lesssim 1\,M_\odot$). In these systems, the mass-transfer mechanism is the Roche lobe overflow (Frank et al. 2002). The transferred matter has angular momentum and forms an accretion disk rather than directly infalling onto the compact object (Pringle & Rees 1972). Matter in the bulk of the disk rotates in Keplerian orbits and slowly diffuses inward, while the angular momentum is transported outward by turbulent viscous processes (Shakura & Sunyaev 1973).

If the accreting object is an NS, the inner parts of the disk may be disrupted at a location beyond the stellar surface. The location of the inner radius of the disk, R_{in}, is determined by the balance between the material and magnetic stresses in the disk (Ghosh & Lamb 1979a, 1979b), which in turn depend on the mass inflow rate $\dot{M}$ in the disk, the magnetic dipole moment μ_*, and the spin angular velocity Ω_* of the star (Lamb et al. 1973). Such magnetized star–disk systems (see Romanova & Owocki 2015 for a review) may show three different stages depending on the relation between the inner radius of the disk and the other two characteristic radii (the corotation radius $R_c = (GM_*/\Omega_*^2)^{1/3}$ and the radius of the light cylinder $R_L = c/\Omega_*$ (Lipunov et al. 1992), where G is the gravitational constant, c is the speed of light, and M_* is the mass of the star):

1. The accretion stage, in which $R_{in} < R_c$, resulting in most (if not all) of the mass flux in the disk reaching the surface of the NS.
2. The propeller stage (Illarionov & Sunyaev 1975), in which $R_c < R_{in} \lesssim R_L$, resulting in none (if not a small fraction) of the inflowing mass reaching the surface of the

NS due to a centrifugal barrier formed by the rapidly rotating magnetosphere.
3. The radio pulsar stage, in which R_{in} is even further away from the star, possibly larger than R_L.

The gravitational potential energy of the infalling material powers the X-ray luminosity,

$$L_X = GM_*\dot{M}_*/R_* \qquad (1)$$

(Davidson & Ostriker 1973), where R_* is the radius of the NS. Here $\dot{M}_*$ is the mass accretion rate onto the NS, and this may be different than the mass flow rate in the disk, $\dot{M}$, in unsteady regimes such as that occurring during an outburst.

Accreting millisecond X-ray pulsars (AMXPs; Wijnands & van der Klis 1998) constitute a subclass of LMXB systems that show coherent pulsations in their X-ray light curves resulting from accretion onto the magnetic pole of an NS from a disk truncated by magnetic stresses (see Patruno & Watts 2012 for a review). All AMXPs are transient systems showing outbursts in their X-ray light curves. A typical X-ray light curve of an outburst displays a fast rise and an exponential decay. Following the released energy during an outburst, a spectral-state transition is realized from the low–hard state (lower luminosity, harder spectrum) to the high–soft state (higher luminosity, softer spectrum) and vice versa. In the hard state, the spectrum is outweighed by hard/Comptonized component with a soft/thermal component, and, in the soft state, the spectrum is more dominated by a soft/thermal component (Lin et al. 2007). Accordingly, $\dot{M}$ rises steeply and declines slowly during the outburst within several weeks, while the magnetic dipole moment and angular velocity of the NS are relatively constant. As $\dot{M}$ changes, these systems may manifest the abovementioned stages of disk-magnetosphere interaction.

AMXPs may thus serve as a lab for exploring the transitions between these different stages.

The decay stage of the X-ray light curves of AMXPs shows a "knee" marking the transition from a slow-decline to a rapid-decline stage (e.g., Ibragimov & Poutanen 2009). The cause of this change in the light curve was suggested to be a transition from the accretion stage to the propeller stage (Campana et al. 1998; Gilfanov et al. 1998; Zhang et al. 1998; Asai et al. 2013), as assumed in this work. Similar "knees" in the light curves are seen in black hole binaries that do not have magnetic fields and cannot show propeller effects. Such transitions are assumed in some other references to be due to the thermal disk instability model (see Lasota 2001 for a review). The pulsations of SAX J1808.4–3658 are detected even at very low luminosities at which the system would be expected to be well within the propeller stage (Menou et al. 1999; Romanova et al. 2004; Ustyugova et al. 2006). This may indicate that the "propeller effect" is not ideal but that a fraction,

$$f \equiv \dot{M}_*/\dot{M}, \qquad (2)$$

of the inflowing mass reaches the surface of the star (Cui 1997; Campana et al. 2001; Asai et al. 2013). This fraction would be a function of the fastness parameter of the system,

$$\omega_* \equiv \Omega_*/\Omega_{\mathrm{K}}(R_{\mathrm{in}}) = (R_{\mathrm{in}}/R_{\mathrm{c}})^{3/2} \qquad (3)$$

(Elsner & Lamb 1977), where $\Omega_{\mathrm{K}} = \sqrt{GM/R^3}$ is the Keplerian angular velocity in the disk. In the simplest picture of an ideal propeller surrounded by an infinitely thin disk, f is a step function:

$$f(\omega_*) = \begin{cases} 1, & \text{for } \omega_* \leqslant 1 \\ 0, & \text{for } \omega_* > 1 \end{cases} \qquad \text{ideal propeller.} \qquad (4)$$

In real disks with a finite scale height, H, a regime of partial accretion may be realized in which f is expected to change smoothly with ω_*. This is because accretion can proceed from higher latitudes of the disk even while the disk midplane is propelled (Romanova et al. 2004; Ekşi & Kutlu 2011). Indeed, the disk may become thicker to allow for such accretion as the fastness parameter goes above unity, or transition to the propeller stage may be induced as a result of the evaporation and thickening of the inner disk (Güngör et al. 2014). The smoothness of the transition will be a measure of $H(R_{\mathrm{in}})/R_{\mathrm{in}}$. Being a dimensionless function of a dimensionless parameter, $f = f(\omega_*)$ should be unique for different outbursts of a system. In general, f may also depend on the inclination angle between the rotation and magnetic axis and so may vary for different systems. Theoretical estimates for $f(\omega_*)$ were presented by Lipunov & Shakura (1976) for spherical accretion and Menou et al. (1999) for the quasi-spherical disk accretion case. The latter authors showed that $f = (3/8)\omega_*^{-4}$ at the $\omega_* \gg 1$ limit. The general case was investigated by Ekşi & Kutlu (2011) with an application to SAX J1808.4–3658, another AMXP. In the present work, we attempt to extract $f = f(\omega_*)$ from observations for the first time in the literature, to our knowledge.

Aql X–1 is one of the most active LMXBTs, exhibiting about 25 outbursts from 1996 until 2016 (Maitra & Bailyn 2008; Asai et al. 2013; Campana et al. 2013; Güngör et al. 2017; Meshcheryakov et al. 2017). Over 20 yr of observations of Aql X–1, the pulsations were observed only in a very short duration of 150 s, which means the source is classified as an intermittent AMXP. The observed spin frequency of $\nu_* = 550.27$ Hz (Casella et al. 2008) and the observations of Type I X-ray bursts (Koyama et al. 1981) firmly establish that the compact object in this system is an NS.

In this work, we investigate *Rossi X-Ray Timing Explorer*/ proportional counter-array (*RXTE*/PCA) observations of Aql X–1 to study the transition into and from the accretion regime to the propeller regime with the assumption that the outbursts of Aql X–1 happen as a result of viscous thermal instability. In Section 2, we explain the details of the data reduction procedures and present their outcomes. In Section 3, we present the method we use to infer $f(\omega_*)$ from the X-ray light curves. In Section 4, we apply the method to the outcomes of our observational analysis and present the results. Finally, in Section 5, we discuss our results and conclude.

2. Observation and Data Analysis

The detected X-ray luminosity is assumed to originate from the NS surface and the inner parts of the disk. In order to separate these two components, we performed a spectral analysis of *RXTE*/PCA observations for the 2000 and 2011 outbursts (52 and 51 pointed observations, respectively). We eliminated observations with thermonuclear bursts and those with very low S/N. The average exposure times of the selected observations were ∼1800 and ∼1450 s, respectively. These observations cover the entire duration of both outbursts, i.e., the fast-rising, slow-decay, and fast-decay phases.

We analyzed the *RXTE*/PCA data using HEASOFT[4] version 6.17. Since Aql X–1 is a very bright source in the X-ray band, we used only the proportional counter unit (PCU2), which was always operational in all pointings. We generated the response files for each observation using PCARSP version 11.7.1, and we used the latest module file[5] for the background model.

All spectra were modeled in the 3.0–30.0 keV range using the XSPEC package.[6] We added a 1.0% systematic error to the data during the χ^2 test to take into account systematic instrumental uncertainties. We hypothesized two different models to represent the spectrum. We first modeled all spectra using a combination of blackbody, disk blackbody, and a Gaussian component to account for fluorescent iron emission. Second, we took the Comptonization into account with the assumption that the NS surface and the Comptonization cloud have the same temperature.

2.1. Model I: Blackbody Assumption

The blackbody component (*bbody* in XSPEC) represents the X-ray emission originating from the hot spot at the pole of the NS fed by accretion. The disk blackbody component (*diskbb* in XSPEC) represents the X-ray contribution of the inner layers of the accretion disk. After determining the best-fit parameters for the blackbody + disk blackbody model for the *RXTE*/PCA data, a Gaussian line was added to represent the iron line. We used a constant neutral hydrogen column density of $N_{\mathrm{H}} = 3.4 \times 10^{21}$ atoms cm^{-2} (Maccarone & Coppi 2003) using the model by Balucinska-Church & McCammon (1992; *phabs* in XSPEC). In Figure 1, we show an example of the fits
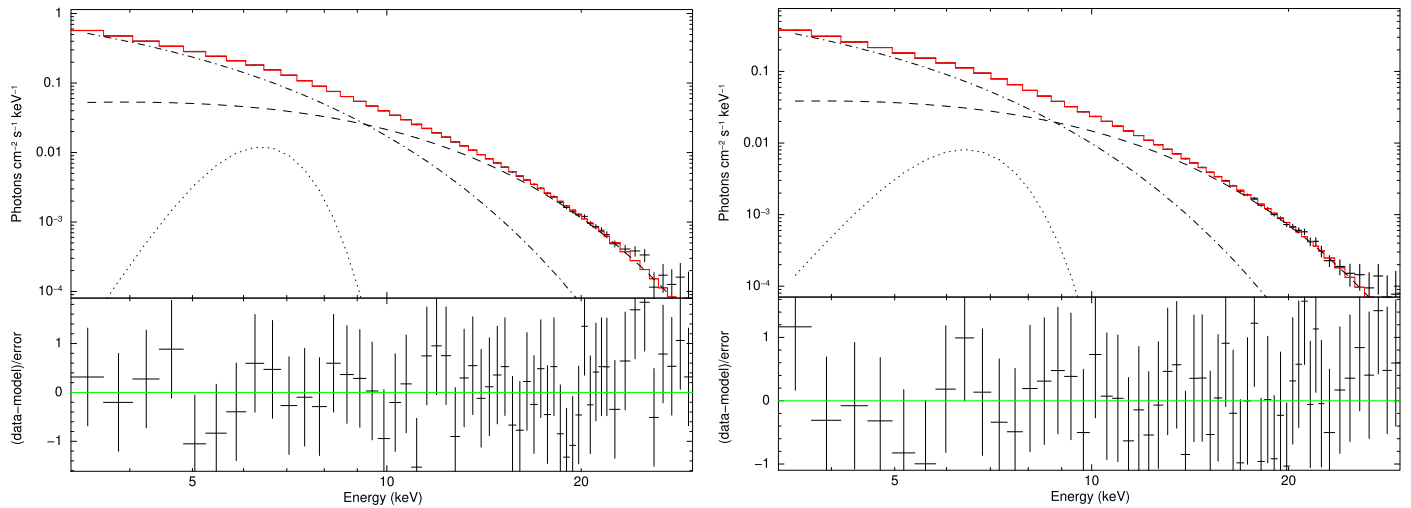
Figure 1. X-ray spectrum of Aql X–1 during outburst, obtained by *RXTE*/PCA in the 3.0–30.0 keV energy range during the 2000 (ObsID 50049-02-08-03, left panel) and 2011 (ObsID 96440-01-05-01, right panel) outbursts. The best fits obtained by using the *bb+diskbb+(ga)* model are shown with red lines. The lower panels show the residuals in terms of σ. The dashed, dash-dotted, and dotted black curves show the blackbody, disk blackbody, and Gaussian components, respectively.

we performed for each data set. A typical normalization value of the *diskbb* component is around $(R_{in}/D_{10})^2 \cos\theta = 100$ (for ObsID 50049-02-08-03), where R_{in} is the inner radius of the disk in km, D_{10} is the distance in units of 10 kpc, and θ is the viewing angle of the disk, giving $R_{in} = 4.5 \, \text{km}/\sqrt{\cos\theta}$, assuming that the source is at 4.5 kpc (Galloway et al. 2008). This value of R_{in} is smaller than the typical radius of an NS for a face-on disk ($\theta = 0$) and reaches reasonable values for $\theta \gtrsim 75°$ corresponding to an almost edge-on view. The reason for a small inner radius may also be an indication that Comptonization is significant (Lin et al. 2007) and the components are not fully separated as we assume.

We calculated the unabsorbed fluxes for the best fit of the X-ray spectra using the blackbody + disk blackbody + Gaussian model for the blackbody and disk blackbody components separately in the range of 3.0–30.0 keV (F_{3-30}) for *RXTE*/PCA data. The bottom panels of Figures 2 and 3 show the light curves for each component for the 2000 and 2011 outburst, respectively.

Moreover, by taking the pivot energy (E_{pivot})—the energy we used to calculate hardness parameter—as 10 keV, we computed the fluxes for the 3.0–10.0 keV (F_{3-10}) and 10.0–30.0 keV (F_{10-30}) energy ranges, following Zhang et al. (1998). We then obtained the hardness evolution using the ratio of F_{10-30}/F_{3-10} (middle panels of Figures 2 and 3). The free parameters of the blackbody and disk blackbody are the temperature of the blackbody component (T_{bb}), the inner disk temperature of the disk blackbody component ($T_{diskbb}(R_{in})$), and the normalizations of the models. We show the evolution of T_{bb} (left) and $T_{diskbb}(R_{in})$ (right) in keV in the top panels of Figures 2 and 3. We provide the final model parameters in Tables 2 and 3 for the 2000 and 2011 observations, respectively.

In both components, we see that the spectral parameters evolve in a similar way. With the commencement of the outburst, T_{bb} drops to ∼2 keV while the hardness ratio of the blackbody decreases to ∼1, and both parameters stay stable during the bright phase of the outburst. It must be mentioned that the resulting temperatures throughout the spectral fits we performed using model I are very high in the low-hard state in which this shows the lack of this model in low-hard state. The hardness decreases to the pre-outburst level before the outburst

ends and the system passes to the quiescent stage. This transition to the rapid-decay stage, rather than to the quiescent stage, marks the transition to the hard state from the soft state (see Remillard & McClintock 2006 for a BH study that is applicable to NSs).

Zhang et al. (1998) argued that the transition in the hardness ratio is caused by the propeller effect (Illarionov & Sunyaev 1975). These critical moments are used to identify the beginning and the terminal of the slow-decay stage and are also used as the fit range in our method described in Section 3.

2.2. Model II: Comptonized Blackbody Assumption

Even though the blackbody assumption works in many cases, the upscattering of the photons by the coronal electrons must also be taken into account. We checked the role of Comptonization by modeling all spectra in the low–hard state and a few examples in the high–soft state corresponding to accretion using a combination similar to that in model I by adding a Comptonization model (*comptTT* in XSPEC; Titarchuk & Lyubarskij 1995) in which the Wien temperature of the Comptonization model is linked to the temperature of the blackbody model under the assumption that photons from the NS surface act as the seed for the inverse Compton process. As is mentioned in Titarchuk (1994), plasma temperature is connected to optical depth and fairly constrained. Thus, plasma temperature is set to a reasonable value: 15.0 keV (Lin et al. 2007).

The geometry is chosen as disk, and the β parameter of Comptonization is obtained from the optical depth (τ) using analytic approximation (see Titarchuk & Lyubarskij 1995 for details). Here τ and the normalization of the Comptonization model are free fit parameters. For the X-ray contribution of the heated inner disk layers, we added the disk blackbody component just as in model I. We added the Gaussian emission-line component with a peak energy of 6.4 keV and maximum σ of 1.0 keV to account for Fe line emission. The input parameters of the disk blackbody component to the fit are taken from the resulting fit of model I to better constrain the Comptonization effect on the blackbody component and to check whether adding Comptonization corrects the high blackbody temperatures in the low–hard state.
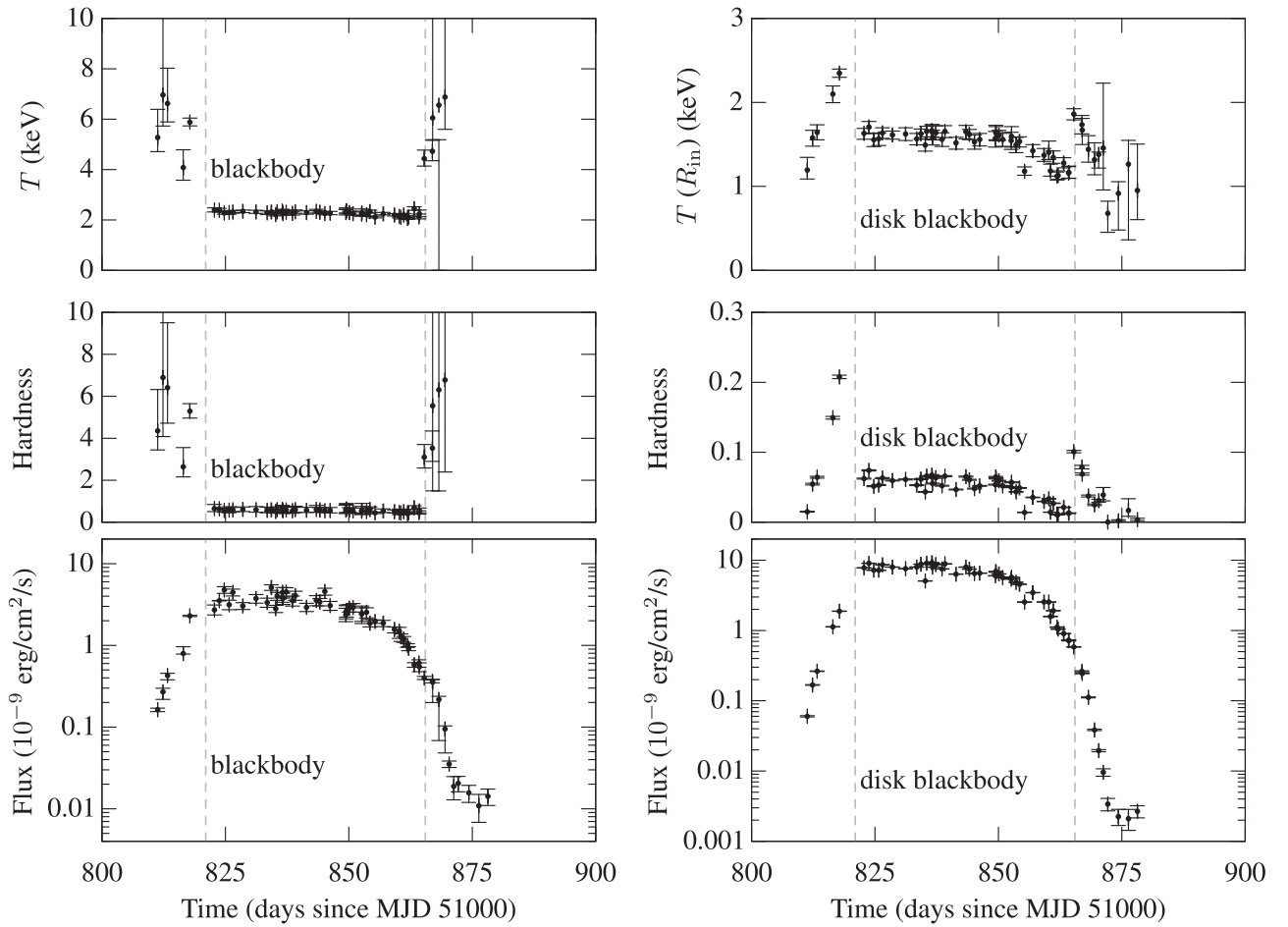
Figure 2. Evolution of spectral parameters during the 2000 outburst of Aql X–1. The top panels show the time evolution of the blackbody temperature (left) and the inner disk temperature of the blackbody (right). The middle panels show the time evolution of the hardness parameter only for the blackbody component (left) and only for the disk blackbody component (right). The bottom panels show the evolution of the flux of the blackbody component (left) and the disk blackbody component (right). The vertical lines show the times of the state transitions.

We provide the resulting parameters of the model II analysis in Tables 4 and 5 for the 2000 and 2011 outbursts, respectively. Model II is preferable to model I for representing the T_{bb} better in the fast-rising phase of the X-ray light curve that corresponds to the low–hard state, since model I gives T_{bb} values that are unphysically high. We tracked the time evolution of τ during outburst. The parameter τ drops to the zero level, following the trend of hardness, indicating that the system changes from the low–hard state to high–soft state. The variance of the parameter τ and hardness of the blackbody component implies that Comptonization becomes ineffective in the high–soft state. It is possible to interpret this simply by suggesting that the contribution of Comptonization during accretion becomes harder to determine when the disk is closer to the star and has an enhanced contribution to the total X-ray flux. The result implies that the blackbody component is sufficient for representing the soft–high state. We will then assume that the light curve of the blackbody component represents the time evolution of the luminosity of accretion onto the NS surface.

3. The Partial Accretion Regime of Outbursts

Here we propose a simple method for extracting $f(\omega_*)$ from the light curve, $L_X(t)$. The method is based on the following assumptions.

1. The rapid-decay stage is a consequence of the transition of the system to the propeller stage $\omega_* > 1$ and is not due to irradiation or any other process.
2. The transition to the propeller stage occurs because material stress declines with accretion rate and hence is balanced by magnetic stresses at a larger distance, now further away from the corotation radius. We note here that BH systems also may have receding inner disk radii, possibly as a result of disk evaporation (see, e.g., Liu et al. 1999; Meyer et al. 2000). If the same mechanism also works in NS systems, a different analysis than ours has to be employed.
3. The decay of the mass inflow rate $\dot{M}$ continues its evolution with no modification upon the transition of the system from accretion to the propeller stage, though a smaller fraction of it can now accrete onto the star, leading to the appearance of rapid decline. This is possibly because of the delay in transferring the information about the changed inner boundary condition to the outer parts of the disk, which keep transporting matter in.
4. The angular velocity Ω_* and magnetic moment μ_* of the NS do not change significantly during an outburst.

We also assume $f = 1$ (meaning that $\dot{M}_* = \dot{M}$) in the slow-decay stage before the knee, though there is reason to believe
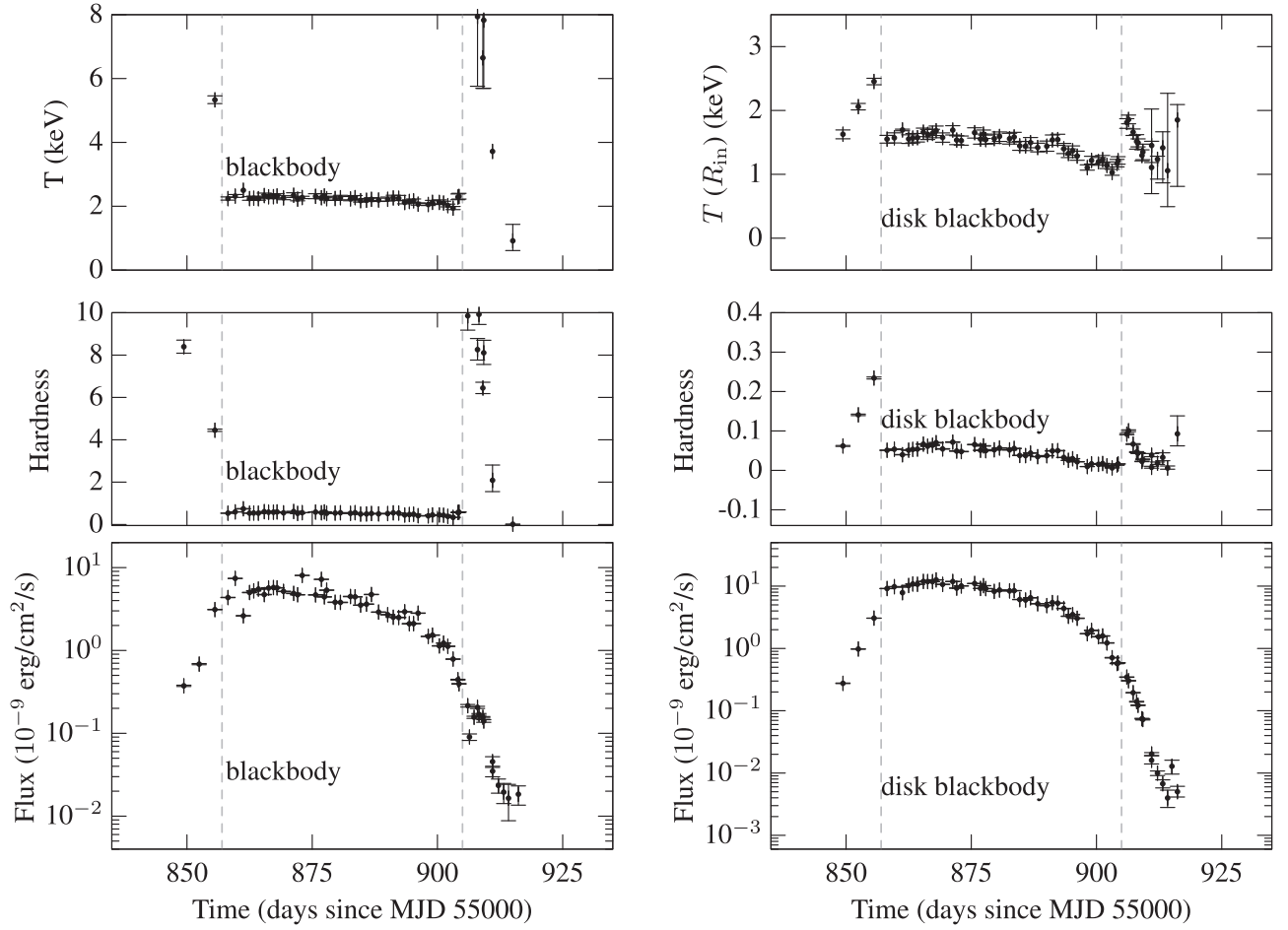
Figure 3. Same as Figure 2, but for the *RXTE*/PCA data during the 2011 outburst of Aql X–1.

that some of the matter donated by the companion is ejected from the disk by winds on the way to the innermost disk. Soon after the maximum is reached, the disk establishes a quasi-equilibrium stage that evolves self-similarly (Lyubarskij & Shakura 1987; Lipunova & Shakura 2002; Suleimanov et al. 2008), where the mass flux will evolve as

$$\dot{M}(t) = \dot{M}_0\left(1 + \frac{t - t_0}{t_\nu}\right)^{-\alpha}. \tag{5}$$

Here t_ν is the timescale of the outburst decay (viscous timescale) and $\dot{M}_0$ is the mass flux at t_0, which is the moment power-law decline starts. In the full accretion regime ($f = 1$), the luminosity follows this trend so that we can fix $\dot{M}_0 = L_0 R_*/GM_*$, where L_0 is the luminosity at the moment of t_0. The value of the power-law index α depends on the pressure and opacity prevailing in the disk (Cannizzo et al. 1990; Ekşi & Kutlu 2011). We have fixed $\alpha = 1.25$ appropriate for a gas pressure–dominated disk with bound-free opacity (Cannizzo et al. 1990). Although the inner parts of the disk for high accretion rates will be dominated by radiation pressure and electron-scattering opacity, the mass flux throughout the disk is regulated by the outer parts where gas-pressure and bound-free opacity dominates.

Aql X–1 is a $\nu_* = \Omega_*/2\pi = 550.27$ Hz AMXP (Casella et al. 2008). The corotation and light cylinder radii for an NS with this spin frequency are $R_c = (GM_*/\Omega_*^2)^{1/3} = 2.5 \times 10^6$ cm

(for $M_* = 1.4\,M_\odot$) and $R_L = c/\Omega_* = 8.7 \times 10^6$ cm, respectively. The maximum critical fastness parameter above which the inner radius goes beyond the light cylinder for this system is $\omega_{*\mathrm{max}} = (R_L/R_c)^{3/2} \simeq 6.5$.

The inner radius of the disk is proportional to the Alfvén radius, $R_{\mathrm{in}} = \xi R_A$, where ξ is a constant of order unity and generally taken as $\xi = 0.5$ (Ghosh & Lamb 1979a, 1979b). The Alfvén radius (Davidson & Ostriker 1973) is

$$R_A = \left(\frac{\mu^2}{\sqrt{2GM\dot{M}}}\right)^{2/7}, \tag{6}$$

where μ is the magnetic dipole moment of the star. This designation could be valid only if it does not yield an inner radius smaller than the radius of the NS. The disk could extend to the surface of the star only at the peak of the brightest outbursts. The Alfvén radius scales with the mass flux as $R_A \propto \dot{M}^{-2/7}$, which then implies, by Equation (3), that $\omega_* \propto \dot{M}^{-3/7}$, or rather

$$\omega_* = (\dot{M}/\dot{M}_c)^{-3/7}, \tag{7}$$

where $\dot{M}_c$ is the mass inflow rate that would place the inner radius on the corotation radius and is related to L_c, the critical luminosity at which partial accretion starts, as $\dot{M}_c = L_c R_*/GM_* f_c$, where f_c is the fraction of mass flux at this critical stage. This corresponds to the luminosity at which rapid decline commences. The inner radius of the disk in the quiescent stage at which $\dot{M} = 0$ was
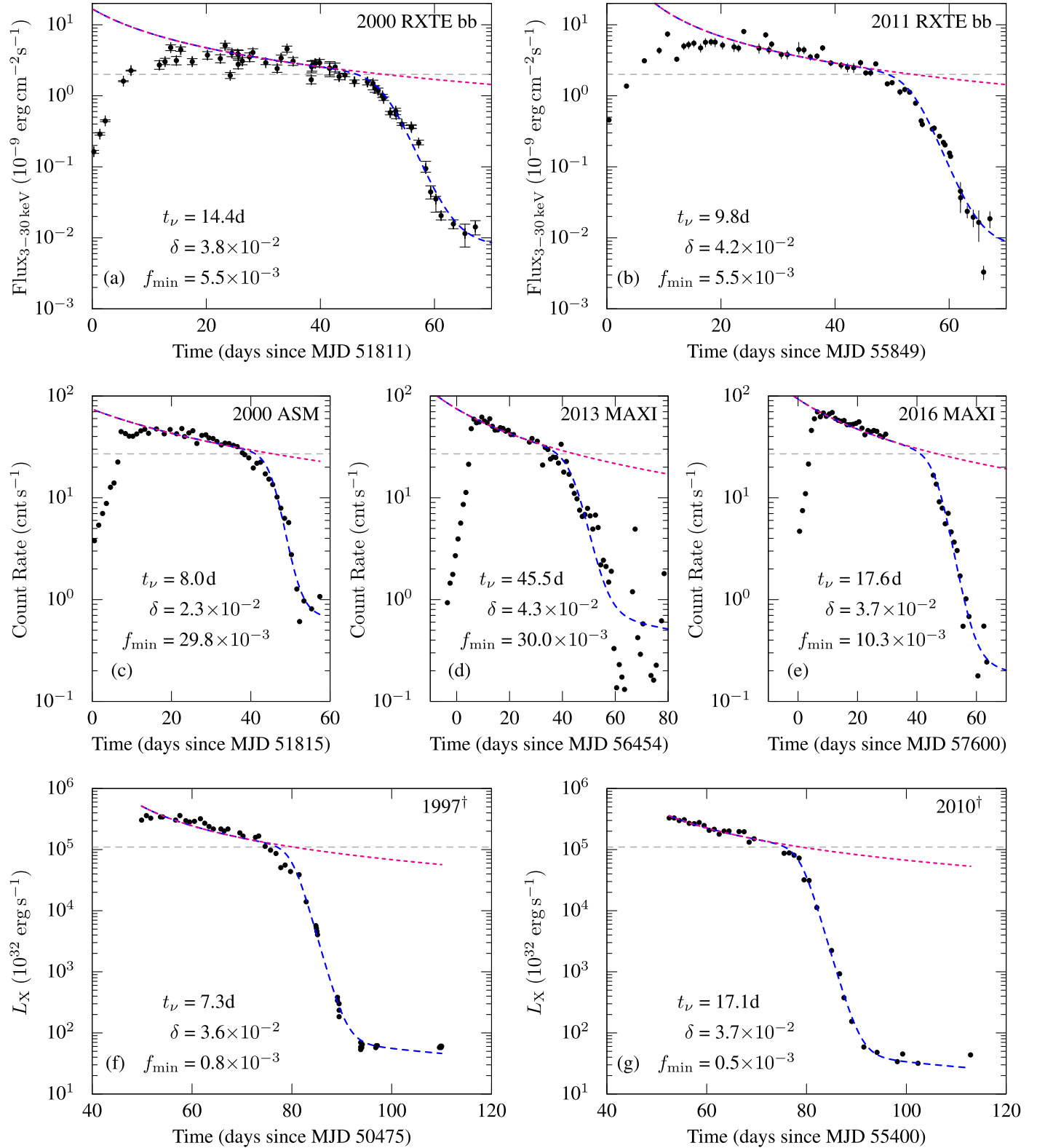
Figure 4. X-ray light curves of the blackbody components of the *RXTE*/PCA data of the (a) 2000 and (b) 2011 outbursts, (c) the ASM light curve of the 2000 outburst, and the MAXI light curves of the (d) 2013 and (e) 2016 outbursts (count rates are calibrated to ASM level). The horizontal lines show the L_c levels in Equation (5). The pink lines show the best fits of Equation (5) between the maximum of outbursts and the knee. The blue curves show the best fits to the total data. (The X-ray light curves of the (f) 1997 and (g) 2010 outbursts were obtained from Campana et al. (2014).)

formalized by Özsükan et al. (2014) in the context of a putative supernova debris disk around the Vela pulsar is assumed to be in a strong propeller stage. In the decay stage that we consider here for

Aql X–1, we have already assumed that mass keeps inflowing even for $\omega_* > 1$ and the system is in a weak propeller regime, so we find the scaling of the Alfvén radius appropriate.

In the propeller stage, we assume that the mass inflow rate in the disk determining the inner radius continues with the same trend. Thus, if all of this inflowing matter could accrete, we would have a luminosity continuing with the same trend as the accretion stage with no knee. The presence of the knee is assumed to be a consequence of partial accretion in the propeller stage; thus, a fraction f of $\dot{M}$ can accrete. The rest of the material may be ejected from the system completely via jets (Tudose et al. 2009). In order to describe this partial accretion, we replace the fraction $f(\omega_*)$ given in Equation (4) for the ideal propeller with a smoothed step function that varies from unity to $f_{min} < 1$,

$$f = \frac{1}{2}\left[1 + f_{min} + (1 - f_{min})\tanh\left(\frac{\omega_c - \omega_*}{\delta}\right)\right], \qquad (8)$$

where ω_c (=1) is the critical fastness parameter at which the transition between accretion and propeller stages occurs, and δ is a measure of the abruptness of this transition.

We first fit the region between the maximum of the light curve and the knee using Equation (5) to determine t_ν, L_0, t_0, and t_{knee}. We then fit the light curves from the maximum of the outburst to the end of the data using $f(t) = f[\omega_*(t)]$ with the initial fit values. From the latter fit, we obtained the values of f_{min} and δ, which are the free fit parameters.

The above analysis assumes that the X-ray luminosity totally originates from accretion onto the NS. For weakly magnetized NSs, such as Aql X–1, the inner radius of the disk is close to the star and the inner disk may contribute to the X-ray luminosity. To obtain the luminosity due to accretion onto the star alone, one needs to use spectral analysis (Section 2).

We note that there are diverging views of how the propeller stage is realized. D'Angelo & Spruit (2010) argued that the propeller stage at low accretion rates will be realized by matter accumulating at the inner disk rather than being ejected out of the system. This will lead to bursts of enhanced accretion (Spruit & Taam 1993; D'Angelo & Spruit 2011) and steady-state quiescent (dead) disk solutions (Sunyaev & Shakura 1977). The timescale for the bursts is the viscous timescale at the inner disk ($\tau_\nu \sim 1$ ms), which is not resolved in the data we employ in this work. Whether the matter is ejected or retained in the disk, the accretion rate onto the star—and hence the X-ray luminosity—will decline. Therefore, from the point of view of the present work, analyzing the fraction of accreting matter onto the star depending on the fastness parameter remains relevant.

4. Applications

A broad classification of the outbursts of Aql X–1 is presented by Güngör et al. (2014) based on the maximum flux and the duration of the outbursts. Accordingly, Aql X–1 shows three main types of outbursts: (i) long-high outbursts, with an outburst duration of 50–60 days and a maximum flux of 37–61 counts s^{-1}; (ii) medium-low outbursts, with 40–50 days and a maximum flux of 13–25 counts s^{-1}; and (iii) short-low outbursts, with approximately 20 days' duration time and a maximum flux of 17–25 counts s^{-1}.

As we focused on the energetic outbursts after performing the spectral analysis of the *RXTE*/PCA data of the 2000 and 2011 outbursts—both belonging to the long-high class—and obtaining the light curves only for blackbody components explained in Section 2.1, we applied the procedure described in
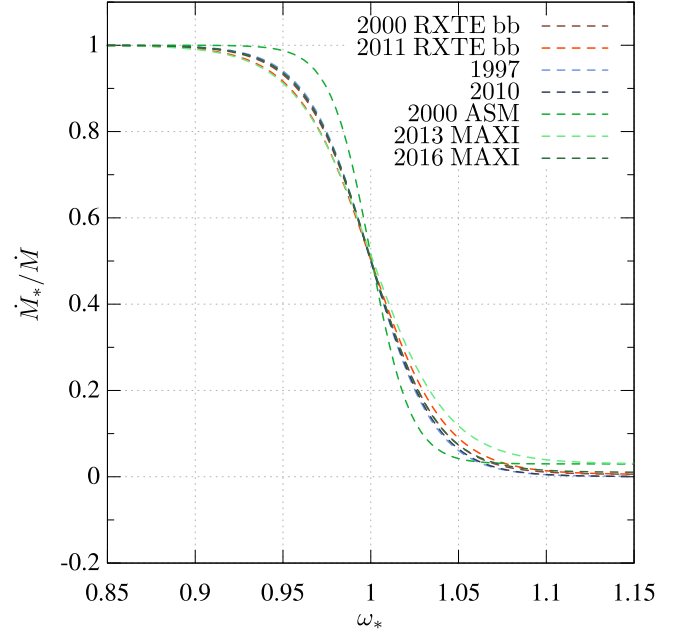
Figure 5. The $f = \dot{M}_*/\dot{M}$ vs. fastness parameter ω_* relation obtained from the outbursts of Aql X–1.

Table 1
Resulting Values of the Free Parameters of the Method

	t_ν (days)	f_{min} (10^{-3})	δ (10^{-2})
2000 *RXTE*	14.4	5.5	3.8
2011 *RXTE*	9.8	5.5[a]	4.2
2000 ASM	8.0	29.8	2.3
2013 MAXI	45.5	30.0[a]	4.3
2016 MAXI	17.6	10.3	3.7
1997[b]	7.3	0.8	3.6
2010[b]	17.1	0.5	3.7

Notes.
[a] The values are fixed to the outcome of the last outburst, since there is not enough data to obtain a base level of the step function.
[b] The light curve data are taken from Campana et al. (2014).

Section 3 to calculate the fraction of mass flux reaching the NS in the propeller stage. In addition, to check the possible differences, we applied the technique to the all-sky monitor (ASM) data of the 2000 outburst, the monitor of the all-sky X-ray image (MAXI) data of the 2013 outburst, and the most energetic one, the 2016 outburst (Güngör et al. 2017).

The decay stages of the 1997 and 2010 outbursts of Aql X–1 have been studied by Campana et al. (1998, 2014). In the latter work, the authors concluded that the rapid-decay stage is likely caused by the transition to the propeller stage. We also applied the method to these outbursts to investigate the mass-transfer characteristic for different classes. In Figure 4, we show the light curves of all outbursts, together with the fit function of Equation (5).

In Figure 5, we show $f \equiv \dot{M}_*/\dot{M}$ versus ω_*, i.e., Equation (8), for all outbursts in our sample. The numerical values of the parameters f_{min} and δ of Equation (8) and t_ν of Equation (5) obtained by fitting the light curve of each outburst (as described in Section 3) are given in Table 1.

Table 2
Best-fit Parameters of the Blackbody + Disk Blackbody + Gaussian Model for the 2000 Outburst

Obs #	ObsID	MJD−51000 (days)	kT_{bbody} (keV)	kT_{diskbb} (keV)	χ^2/dof[a]	Hardness[b] $bbody$	Hardness[b] $diskbb$	Flux$_{bbody}$[c]	Flux$_{diskbb}$[d]
1	50049-01-03-00	811.28564	5.27 ± 1.12	1.19 ± 0.15	0.90	4.36 ± 1.97	1.50 ± 0.06	1.63 ± 0.08	0.60 ± 0.01
2	50049-01-03-01	812.34953	6.96 ± 1.23	1.58 ± 0.10	1.14	6.89 ± 2.81	5.45 ± 0.13	2.70 ± 0.52	1.68 ± 0.02
3	50049-01-03-02	813.27735	6.63 ± 1.40	1.64 ± 0.09	1.00	6.41 ± 1.69	6.43 ± 0.13	4.27 ± 0.49	2.63 ± 0.03
4	50049-01-04-00	816.46667	4.08 ± 0.71	2.10 ± 0.10	1.13	2.64 ± 0.92	14.93 ± 0.20	7.95 ± 1.67	11.29 ± 0.08
5	50049-01-04-01	817.79791	5.88 ± 0.16	2.35 ± 0.05	1.24	5.29 ± 0.36	20.77 ± 0.25	22.94 ± 0.40	18.80 ± 0.11
6	50049-01-04-04	822.77448	2.40 ± 0.08	1.63 ± 0.07	0.69	0.65 ± 0.19	6.23 ± 0.07	27.16 ± 4.01	77.91 ± 0.44
7	50049-01-05-00	823.76888	2.38 ± 0.07	1.71 ± 0.07	0.57	0.64 ± 0.06	7.40 ± 0.14	35.20 ± 0.20	90.30 ± 0.50
8	50049-01-05-01	824.76115	2.28 ± 0.05	1.56 ± 0.08	0.38	0.56 ± 0.11	5.15 ± 0.07	47.76 ± 4.49	72.13 ± 0.48
9	50049-01-05-02	825.75496	2.29 ± 0.08	1.57 ± 0.08	0.63	0.57 ± 0.16	5.31 ± 0.06	31.39 ± 4.32	71.95 ± 0.44
10	50049-02-01-00	826.51291	2.31 ± 0.05	1.64 ± 0.07	0.39	0.59 ± 0.12	6.31 ± 0.07	44.55 ± 4.34	86.14 ± 0.52
11	50049-02-02-00	828.53443	2.34 ± 0.05	1.61 ± 0.05	0.75	0.61 ± 0.12	5.96 ± 0.06	30.32 ± 3.03	79.80 ± 0.45
12	50049-02-03-01	831.20242	2.32 ± 0.07	1.62 ± 0.08	0.49	0.59 ± 0.15	6.12 ± 0.07	37.45 ± 4.64	75.74 ± 0.46
13	50049-02-03-00	833.45856	2.28 ± 0.07	1.57 ± 0.07	0.81	0.57 ± 0.15	5.30 ± 0.06	33.46 ± 4.39	79.95 ± 0.47
14	50049-02-04-00	834.30025	2.31 ± 0.04	1.63 ± 0.06	0.31	0.59 ± 0.09	6.16 ± 0.08	51.16 ± 4.02	87.91 ± 0.55
15	50049-02-03-02	835.19034	2.21 ± 0.06	1.49 ± 0.07	0.40	0.51 ± 0.11	4.33 ± 0.06	28.15 ± 2.96	50.67 ± 0.33
16	50049-02-05-00	835.47605	2.32 ± 0.06	1.65 ± 0.07	0.30	0.59 ± 0.14	6.58 ± 0.07	40.02 ± 4.54	90.68 ± 0.52
17	50049-02-06-00	836.51501	2.35 ± 0.08	1.66 ± 0.08	0.45	0.62 ± 0.18	6.73 ± 0.08	38.97 ± 5.37	92.11 ± 0.52
18	50049-02-06-01	836.59062	2.31 ± 0.08	1.65 ± 0.09	0.61	0.58 ± 0.19	6.47 ± 0.08	44.63 ± 6.76	89.74 ± 0.55
19	50049-02-06-02	836.65903	2.25 ± 0.09	1.58 ± 0.09	0.41	0.54 ± 0.19	5.53 ± 0.07	37.83 ± 6.14	79.84 ± 0.50
20	50049-02-07-00	837.31072	2.30 ± 0.07	1.64 ± 0.09	0.59	0.58 ± 0.16	6.34 ± 0.08	45.08 ± 5.90	86.81 ± 0.54
21	50049-02-07-01	838.58253	2.26 ± 0.08	1.56 ± 0.08	0.78	0.55 ± 0.16	5.21 ± 0.07	35.25 ± 4.99	75.20 ± 0.47
22	50049-02-07-02	839.16547	2.33 ± 0.07	1.66 ± 0.07	0.38	0.60 ± 0.16	6.59 ± 0.08	40.72 ± 5.23	88.67 ± 0.51
23	50049-02-07-03	841.42330	2.29 ± 0.07	1.52 ± 0.08	0.83	0.57 ± 0.14	4.67 ± 0.06	29.26 ± 3.45	63.35 ± 0.40
24	50049-02-07-04	843.42348	2.34 ± 0.08	1.65 ± 0.08	0.47	0.61 ± 0.19	6.52 ± 0.08	35.51 ± 5.09	79.77 ± 0.46
25	50049-02-08-00	844.12055	2.31 ± 0.05	1.62 ± 0.06	0.44	0.58 ± 0.13	6.06 ± 0.07	33.90 ± 3.53	74.70 ± 0.44
26	50049-02-08-01	845.14572	2.25 ± 0.06	1.53 ± 0.09	0.29	0.54 ± 0.11	4.80 ± 0.07	45.79 ± 4.64	64.78 ± 0.45
27	50049-02-08-03	846.20867	2.27 ± 0.07	1.56 ± 0.08	0.47	0.55 ± 0.15	5.20 ± 0.06	30.71 ± 3.89	65.45 ± 0.42
28	50049-02-10-03	849.39406	2.29 ± 0.11	1.57 ± 0.10	0.48	0.57 ± 0.24	5.37 ± 0.06	23.76 ± 4.69	60.09 ± 0.37
29	50049-02-10-02	849.46316	2.36 ± 0.11	1.65 ± 0.09	0.79	0.63 ± 0.26	6.47 ± 0.07	25.65 ± 4.95	68.85 ± 0.40
30	50049-02-10-01	849.53465	2.36 ± 0.11	1.63 ± 0.09	0.89	0.62 ± 0.24	6.26 ± 0.07	26.61 ± 4.62	67.68 ± 0.40
31	50049-02-10-00	850.10229	2.29 ± 0.05	1.61 ± 0.06	0.38	0.57 ± 0.12	5.92 ± 0.07	28.52 ± 2.95	63.79 ± 0.36
32	50049-02-10-05	850.86400	2.25 ± 0.06	1.56 ± 0.08	0.72	0.54 ± 0.14	5.18 ± 0.06	29.09 ± 3.53	56.65 ± 0.36
33	50049-02-11-01	852.58772	2.23 ± 0.11	1.54 ± 0.10	1.13	0.53 ± 0.23	5.01 ± 0.06	24.38 ± 4.74	53.92 ± 0.34
34	50049-02-11-02	852.65313	2.28 ± 0.16	1.60 ± 0.13	0.73	0.56 ± 0.34	5.70 ± 0.07	24.49 ± 5.96	57.21 ± 0.37
35	50049-02-12-01	853.58329	2.21 ± 0.09	1.49 ± 0.09	0.57	0.51 ± 0.15	4.35 ± 0.06	25.43 ± 3.74	48.45 ± 0.33
36	50049-02-12-00	854.27232	2.33 ± 0.06	1.54 ± 0.07	0.76	0.60 ± 0.13	4.90 ± 0.07	18.68 ± 2.09	45.47 ± 0.28
37	50049-02-13-00	855.30361	2.11 ± 0.04	1.18 ± 0.05	0.87	0.45 ± 0.04	1.40 ± 0.02	19.59 ± 0.99	25.38 ± 0.21
38	50049-02-14-00	856.96964	2.25 ± 0.05	1.42 ± 0.07	0.82	0.54 ± 0.10	3.54 ± 0.05	18.73 ± 1.78	34.56 ± 0.24
39	50049-02-15-00	859.24090	2.20 ± 0.05	1.37 ± 0.07	0.99	0.50 ± 0.08	2.97 ± 0.04	15.66 ± 1.44	25.45 ± 0.19
40	50049-02-15-01	860.21521	2.14 ± 0.10	1.41 ± 0.13	0.63	0.46 ± 0.16	3.35 ± 0.05	14.95 ± 2.78	25.42 ± 0.19
41	50049-02-15-08	860.54742	2.10 ± 0.10	1.18 ± 0.08	1.01	0.44 ± 0.10	1.43 ± 0.03	12.74 ± 1.58	15.82 ± 0.15
42	50049-02-15-02	861.11940	2.20 ± 0.06	1.34 ± 0.08	1.12	0.50 ± 0.08	2.71 ± 0.04	11.94 ± 0.89	19.12 ± 0.15
43	50049-02-15-03	861.88606	2.06 ± 0.04	1.12 ± 0.05	0.84	0.41 ± 0.04	1.05 ± 0.02	9.99 ± 0.53	11.14 ± 0.10
44	50049-02-15-04	862.09305	2.11 ± 0.05	1.13 ± 0.05	1.35	0.45 ± 0.05	1.10 ± 0.02	9.18 ± 0.57	10.45 ± 0.10
45	50049-02-15-05	863.23997	2.45 ± 0.08	1.28 ± 0.06	1.72	0.70 ± 0.09	2.13 ± 0.03	5.78 ± 0.39	9.03 ± 0.08
46	50049-02-15-06	864.20819	2.12 ± 0.11	1.16 ± 0.08	0.83	0.45 ± 0.10	1.27 ± 0.03	6.07 ± 0.67	7.24 ± 0.07
47	50049-02-15-07	864.27747	2.24 ± 0.15	1.17 ± 0.08	0.85	0.54 ± 0.14	1.31 ± 0.03	5.46 ± 0.70	7.19 ± 0.08
48	50049-03-01-00	865.27217	4.43 ± 0.34	1.86 ± 0.07	1.48	3.10 ± 0.61	10.09 ± 0.17	3.99 ± 0.17	5.83 ± 0.05
49	50049-03-02-01	866.92250	4.73 ± 0.46	1.74 ± 0.11	0.99	3.53 ± 0.63	7.87 ± 0.25	3.64 ± 0.16	2.63 ± 0.04
50	50049-03-02-00	866.97790	6.05 ± 0.89	1.67 ± 0.17	0.96	5.55 ± 4.06	6.88 ± 0.15	3.55 ± 1.55	2.45 ± 0.03
51	50049-03-03-00	868.23607	6.56 ± 1.37	1.44 ± 0.16	0.74	6.31 ± 4.82	3.75 ± 0.14	2.17 ± 1.49	1.12 ± 0.02
52	50049-03-04-00	869.47435	6.88 ± 1.28	1.32 ± 0.20	0.86	6.78 ± 4.38	2.49 ± 0.11	0.95 ± 0.47	0.38 ± 0.01

Notes. The horizontal lines in the table indicate the state transitions according to the hardness parameter of the blackbody component.
[a] The degree of freedom (dof) is 48 for all observations.
[b] Hardness parameters are obtained using the flux ratio of two different energy ranges: $F(10–30\,\mathrm{keV})/F(3–10\,\mathrm{keV})$. The parameters for the $diskbb$ component are multiplied by 10^2 because of low values.
[c] Unabsorbed fluxes of the blackbody components are in units of 10^{-10} erg s^{-1} cm^{-2}.
[d] Unabsorbed fluxes of the disk blackbody components are in units of 10^{-10} erg s^{-1} cm^{-2}.

Table 3
Same as Table 2, but for the 2011 Outburst

Obs #	ObsID	MJD−55000 (days)	kT_{bbody} (keV)	kT_{diskbb} (keV)	χ^2/dof[a]	Hardness[b] bbody	Hardness[b] diskbb	Flux$_{bbody}$[c]	Flux$_{diskbb}$[d]
1	96440-01-01-00	849.3771	8.04 ± 1.71	1.63 ± 0.07	1.09	8.39 ± 0.32	6.19 ± 0.12	3.74 ± 0.07	2.76 ± 0.03
2	96440-01-01-01	852.4442	12.11 ± 4.58	2.06 ± 0.05	0.98	12.77 ± 0.42	14.08 ± 0.19	6.83 ± 0.11	9.78 ± 0.06
3	96440-01-02-02	855.5727	5.33 ± 0.13	2.45 ± 0.05	1.11	4.45 ± 0.06	23.44 ± 0.26	31.11 ± 0.19	30.63 ± 0.17
4	96440-01-02-00	858.1840	2.24 ± 0.05	1.55 ± 0.06	0.60	0.53 ± 0.01	5.10 ± 0.06	43.52 ± 0.25	91.63 ± 0.54
5	96440-01-02-03	859.6329	2.32 ± 0.05	1.57 ± 0.08	0.54	0.59 ± 0.01	5.36 ± 0.07	74.03 ± 0.41	98.06 ± 0.69
6	96440-01-02-01	861.2549	2.50 ± 0.03	1.69 ± 0.01	1.10	0.74 ± 0.01	3.97 ± 0.20	26.10 ± 0.51	78.60 ± 0.34
7	96440-01-03-02	862.4965	2.24 ± 0.06	1.55 ± 0.07	0.54	0.53 ± 0.01	5.12 ± 0.06	50.02 ± 0.32	102.58 ± 0.63
8	96440-01-03-05	863.3270	2.25 ± 0.07	1.57 ± 0.07	0.71	0.54 ± 0.01	5.32 ± 0.07	52.41 ± 0.35	108.54 ± 0.67
9	96440-01-03-00	864.2559	2.24 ± 0.06	1.57 ± 0.07	0.61	0.53 ± 0.01	5.41 ± 0.07	54.97 ± 0.32	107.14 ± 0.65
10	96440-01-03-03	865.4324	2.34 ± 0.08	1.66 ± 0.06	0.42	0.61 ± 0.01	6.66 ± 0.07	47.21 ± 0.33	119.18 ± 0.65
11	96440-01-03-06	866.2909	2.30 ± 0.08	1.63 ± 0.08	0.52	0.58 ± 0.01	6.14 ± 0.07	56.66 ± 0.40	118.43 ± 0.73
12	96440-01-03-01	867.2569	2.30 ± 0.06	1.64 ± 0.06	0.38	0.58 ± 0.01	6.37 ± 0.07	57.38 ± 0.32	118.24 ± 0.68
13	96440-01-03-04	867.9826	2.32 ± 0.07	1.68 ± 0.07	0.37	0.60 ± 0.01	7.02 ± 0.08	56.88 ± 0.37	125.92 ± 0.74
14	96440-01-04-03	869.2781	2.26 ± 0.07	1.58 ± 0.07	0.53	0.55 ± 0.01	5.44 ± 0.07	51.59 ± 0.35	106.77 ± 0.65
15	96440-01-04-04	871.2958	2.35 ± 0.08	1.69 ± 0.07	0.55	0.61 ± 0.01	7.16 ± 0.08	48.77 ± 0.33	118.72 ± 0.66
16	96440-01-04-01	872.0858	2.22 ± 0.06	1.54 ± 0.07	0.41	0.52 ± 0.01	4.90 ± 0.06	46.96 ± 0.29	93.05 ± 0.57
17	96440-01-04-05	873.0034	2.27 ± 0.04	1.53 ± 0.07	0.49	0.56 ± 0.01	4.78 ± 0.07	80.36 ± 0.41	100.79 ± 0.74
18	96440-01-04-06	875.6732	2.31 ± 0.08	1.65 ± 0.08	0.56	0.59 ± 0.01	6.55 ± 0.07	46.82 ± 0.32	110.27 ± 0.61
19	96440-01-05-00	876.8402	2.27 ± 0.04	1.55 ± 0.08	0.49	0.55 ± 0.01	5.10 ± 0.07	72.06 ± 0.34	91.93 ± 0.64
20	96440-01-05-01	877.4295	2.32 ± 0.07	1.63 ± 0.06	0.59	0.60 ± 0.01	6.21 ± 0.07	44.29 ± 0.29	101.79 ± 0.58
21	96440-01-05-02	877.8880	2.24 ± 0.05	1.54 ± 0.07	0.57	0.53 ± 0.01	5.00 ± 0.06	53.36 ± 0.30	91.42 ± 0.59
22	96440-01-05-03	879.5833	2.24 ± 0.07	1.56 ± 0.07	0.54	0.54 ± 0.01	5.21 ± 0.06	38.17 ± 0.25	82.47 ± 0.49
23	96440-01-05-04	880.6295	2.27 ± 0.08	1.59 ± 0.07	0.70	0.55 ± 0.01	5.67 ± 0.07	38.00 ± 0.26	86.76 ± 0.48
24	96440-01-05-05	882.6413	2.23 ± 0.08	1.56 ± 0.08	0.57	0.53 ± 0.01	5.20 ± 0.07	44.76 ± 0.30	83.84 ± 0.53
25	96440-01-06-00	883.5596	2.27 ± 0.07	1.58 ± 0.07	0.59	0.56 ± 0.01	5.56 ± 0.07	44.31 ± 0.28	84.61 ± 0.51
26	96440-01-06-01	884.6704	2.18 ± 0.05	1.45 ± 0.07	0.88	0.49 ± 0.01	3.79 ± 0.05	35.19 ± 0.21	61.04 ± 0.40
27	96440-01-06-02	885.8371	2.19 ± 0.05	1.44 ± 0.07	0.60	0.50 ± 0.01	3.75 ± 0.05	36.20 ± 0.20	59.89 ± 0.40
28	96440-01-06-03	886.8228	2.22 ± 0.05	1.50 ± 0.08	0.73	0.52 ± 0.01	4.38 ± 0.06	47.34 ± 0.24	65.07 ± 0.42
29	96440-01-06-04	888.2533	2.20 ± 0.06	1.42 ± 0.07	0.65	0.50 ± 0.01	3.48 ± 0.05	29.03 ± 0.17	52.16 ± 0.35
30	96440-01-07-00	890.0729	2.22 ± 0.07	1.44 ± 0.08	0.81	0.52 ± 0.01	3.72 ± 0.05	26.97 ± 0.17	48.77 ± 0.32
31	96440-01-07-01	891.1884	2.26 ± 0.08	1.54 ± 0.08	0.85	0.55 ± 0.01	4.94 ± 0.06	25.15 ± 0.17	54.51 ± 0.32
32	96440-01-07-02	892.2633	2.25 ± 0.09	1.54 ± 0.08	0.41	0.54 ± 0.01	4.99 ± 0.06	24.98 ± 0.17	53.47 ± 0.31
33	96440-01-07-03	893.4686	2.12 ± 0.06	1.40 ± 0.08	0.67	0.45 ± 0.01	3.28 ± 0.05	29.27 ± 0.18	43.78 ± 0.31
34	96440-01-07-04	894.3870	2.15 ± 0.05	1.33 ± 0.07	0.84	0.47 ± 0.01	2.54 ± 0.04	21.01 ± 0.13	32.87 ± 0.23
35	96440-01-07-05	895.2340	2.17 ± 0.06	1.37 ± 0.08	0.72	0.48 ± 0.01	2.95 ± 0.04	21.07 ± 0.13	34.92 ± 0.23
36	96440-01-07-06	896.1426	2.07 ± 0.04	1.29 ± 0.08	0.80	0.41 ± 0.01	2.18 ± 0.04	28.16 ± 0.15	30.50 ± 0.25
37	96440-01-08-00	898.1645	2.06 ± 0.04	1.10 ± 0.04	1.35	0.41 ± 0.01	0.97 ± 0.02	14.75 ± 0.09	17.27 ± 0.15
38	96440-01-08-02	899.0077	2.12 ± 0.06	1.22 ± 0.07	1.54	0.45 ± 0.01	1.65 ± 0.03	15.29 ± 0.11	19.47 ± 0.16
39	96440-01-08-03	900.3845	2.12 ± 0.08	1.20 ± 0.06	1.31	0.45 ± 0.01	1.53 ± 0.03	11.34 ± 0.08	15.41 ± 0.13
40	96440-01-08-04	901.2278	2.10 ± 0.06	1.23 ± 0.07	0.92	0.44 ± 0.01	1.75 ± 0.03	12.26 ± 0.09	15.87 ± 0.12
41	96440-01-08-05	902.0756	2.02 ± 0.05	1.14 ± 0.06	0.78	0.39 ± 0.01	1.15 ± 0.02	11.22 ± 0.08	12.26 ± 0.11
42	96440-01-08-06	903.1209	1.94 ± 0.05	1.03 ± 0.05	0.86	0.34 ± 0.01	0.63 ± 0.01	7.86 ± 0.06	7.10 ± 0.08
43	96440-01-09-00	904.0978	2.29 ± 0.10	1.17 ± 0.06	1.56	0.57 ± 0.01	1.34 ± 0.03	4.44 ± 0.05	5.74 ± 0.05
44	96440-01-09-08	904.3096	2.31 ± 0.10	1.21 ± 0.06	1.35	0.58 ± 0.01	1.63 ± 0.03	3.95 ± 0.04	5.86 ± 0.05
45	96440-01-09-02	906.0508	9.22 ± 3.94	1.81 ± 0.06	0.93	9.85 ± 0.72	9.19 ± 0.17	2.15 ± 0.08	3.47 ± 0.03
46	96440-01-09-03	907.3148	15.80 ± 7.33	1.66 ± 0.05	1.17	15.40 ± 0.96	6.67 ± 0.12	1.56 ± 0.05	1.95 ± 0.02
47	96440-01-09-10	908.0061	7.94 ± 2.18	1.51 ± 0.11	1.03	8.26 ± 0.52	4.63 ± 0.13	2.05 ± 0.06	1.40 ± 0.02
48	96440-01-09-04	908.2906	9.27 ± 2.57	1.49 ± 0.06	1.02	9.92 ± 0.49	4.37 ± 0.09	1.69 ± 0.04	1.22 ± 0.01
49	96440-01-09-05	909.0731	6.65 ± 1.80	1.30 ± 0.09	1.07	6.44 ± 0.27	2.27 ± 0.06	1.56 ± 0.03	0.75 ± 0.01
50	96440-01-09-11	909.2486	7.83 ± 2.14	1.35 ± 0.12	0.84	8.11 ± 0.59	2.78 ± 0.10	1.41 ± 0.05	0.72 ± 0.01
51	96440-01-09-12	910.9905	3.72 ± 3.72	1.11 ± 0.91	0.61	2.09 ± 0.72	0.76 ± 0.27	0.45 ± 0.07	0.16 ± 0.03

Notes.
[a] The degree of freedom (dof) is 49 for all observations.
[b] Hardness parameters are obtained using the flux ratio of two different energy ranges: $F(10–30\,\mathrm{keV})/F(3–10\,\mathrm{keV})$. The parameters for the disk blackbody component are multiplied by 10^2 because of low values.
[c] Unabsorbed fluxes of the blackbody components are in units of $10^{-10}\,\mathrm{erg\,s^{-1}\,cm^{-2}}$.
[d] Unabsorbed fluxes of the disk blackbody components are in units of $10^{-10}\,\mathrm{erg\,s^{-1}\,cm^{-2}}$.

Table 4
Best-fit Parameters of the Blackbody + Comptonization + Disk Blackbody + Gaussian Model for the 2000 Outburst

Obs #	kT_{bbody} (keV)	τ	χ^2/dof[a]	Hardness[b] bbody	Flux$_{bbody}$[c]
1	2.36 ± 0.30	2.72 ± 0.67	0.95	2.77 ± 0.10	1.84 ± 0.02
2	2.80 ± 0.21	2.49 ± 0.30	1.13	3.30 ± 0.09	3.37 ± 0.03
3	2.77 ± 0.21	2.76 ± 0.26	1.03	3.49 ± 0.08	5.10 ± 0.04
4	3.61 ± 0.36	2.38 ± 0.60	0.68	4.73 ± 0.07	16.74 ± 0.07
5	3.44 ± 0.70	2.44 ± 0.16	0.69	4.31 ± 0.06	24.74 ± 0.10
6	2.17 ± 0.13	0.12 ± 0.04	0.63	0.59 ± 0.01	30.91 ± 0.17
7	2.34 ± 0.05	0.01 ± 0.01	0.62	0.65 ± 0.01	34.82 ± 0.20
8	2.24 ± 0.03	0.10 ± 0.02	0.32	0.56 ± 0.01	48.09 ± 0.21
9	2.22 ± 0.05	0.01 ± 0.01	0.68	0.60 ± 0.01	30.65 ± 0.17
10	2.27 ± 0.03	0.01 ± 0.01	0.51	0.60 ± 0.01	44.13 ± 0.20
16	2.25 ± 0.03	0.13 ± 0.09	0.52	0.58 ± 0.01	40.97 ± 0.20
31	2.25 ± 0.04	0.11 ± 0.10	0.49	0.56 ± 0.01	28.96 ± 0.14
39	2.00 ± 0.03	0.06 ± 0.02	0.93	0.48 ± 0.01	16.36 ± 0.07
41	1.91 ± 0.03	0.03 ± 0.02	1.30	0.40 ± 0.01	13.82 ± 0.07
44	1.70 ± 0.06	0.45 ± 0.36	1.74	0.34 ± 0.01	12.04 ± 0.05
45	1.80 ± 0.08	0.48 ± 0.13	1.99	0.49 ± 0.01	7.85 ± 0.03
46	1.95 ± 0.04	0.01 ± 0.01	1.63	0.40 ± 0.01	6.74 ± 0.04
47	2.01 ± 0.15	0.11 ± 0.07	0.80	0.53 ± 0.01	5.65 ± 0.04
48	3.48 ± 0.45	1.63 ± 0.51	1.40	3.27 ± 0.13	4.06 ± 0.05
49	3.75 ± 0.65	2.30 ± 0.88	0.93	3.71 ± 0.19	3.71 ± 0.07
50	2.82 ± 0.40	2.83 ± 0.22	0.91	3.64 ± 0.11	4.00 ± 0.04
51	2.72 ± 0.48	2.84 ± 0.85	0.67	3.47 ± 0.15	2.49 ± 0.04
52	2.55 ± 0.56	2.98 ± 0.20	0.78	3.29 ± 0.15	1.07 ± 0.02

Notes. The horizontal lines in the table indicate the state transitions according to the hardness parameter of the blackbody component.
[a] The degree of freedom (dof) is 49 for all observations.
[b] Hardness parameters are obtained using the flux ratio of two different energy ranges: $F(10–30 \text{ keV})/F(3–10 \text{ keV})$.
[c] Unabsorbed fluxes of the blackbody components are in units of $10^{-10} \text{ erg s}^{-1} \text{ cm}^{-2}$.

5. Discussion

In this paper, we studied the evolution of the disk-magnetosphere interaction from accretion to the propeller regime using the X-ray data of Aql X–1.

We analyzed the *RXTE*/PCA data of the 2000 and 2011 outbursts of Aql X–1. We modeled each spectrum using a combination of blackbody and disk blackbody and obtained the light curves and time evolution of the spectral parameters for each component separately.

The blackbody component represents seed photons released at the hot spot on the NS poles while Comptonization plays a role in the spectral formation. We checked the validity of the blackbody assumption using a Comptonization model (*comptTT* in XSPEC; Titarchuk & Lyubarskij 1995) with a linked Wien temperature parameter to the blackbody temperature and showed that Comptonization is not significantly dominant during the slow-decay stage. This supports the view that X-ray flux due to accretion is represented by blackbody radiation. Different models could be employed to separate the contributions of different components to the total X-ray flux (e.g., *nthcomp (blackbody)+diskbb*; Lin et al. 2007; Sakurai et al. 2012).

Although Comptonization is ineffective in the soft state, adding it to the model corrects the blackbody temperatures in the hard state. Temperatures inferred without employing Comptonization are too high to be explained via known physical processes (Obs # 1–5 in Table 2 and Obs # 1–3 in Table 3). The last two data of the hard state, however, show similarly high temperatures even with the Comptonization component included (Obs # 4, 5 in Table 4 and Obs # 2, 3 in

Table 5). These data correspond to the episode before the maximum of the X-ray light curve, and the spectra at this episode are still hard while the luminosity is high. This may indicate a high–hard interstage that occurs at the rising stage of the outburst before the low–hard stage and high–soft stage at the decay stages. Considering that a similar situation exists in transitions from the high–soft stage to low–hard stage (Obs # 48, 49 in Table 4 and Obs # 45, 46 in Table 5), we suggest that the system shows a pre-propeller stage at a similar luminosity level while the disk drifts to the inner layers. As the rising phase of the X-ray light curve is shorter than the decay phase, the pre-propeller stage is shorter than the propeller stage.

Recently, Tsygankov et al. (2017) suggested that the decline in X-ray flux during the outbursts of high-mass X-ray binary systems (containing slowly rotating NSs) is due to transition to a cold (neutral; $T \lesssim 6500$ K) disk state. In this case, the accretion rate is low due to the suppression of magnetorotational instabilities. In the case of Aql X–1, the rapid rotation and relatively small magnetic field of the compact object will likely eliminate the possibility of accretion from a cold disk (see Figure 3 of Tsygankov et al. 2017).

For probing the transitions from the accretion to the propeller stage, we introduced a novel method to determine the ratio of the mass accretion rate onto the NS pole to the mass inflow rate at the inner disk, depending on the fastness parameter, from the observed X-ray light curve. The method depends on the assumptions that the rapid-decay stage corresponds to the propeller stage at which partial accretion proceeds and that the X-ray flux is due to weak accretion onto the poles. Our results imply a steeper decline of f with the fastness parameter

Table 5
Same as Table 4, but for the 2011 Outburst

Obs #	kT_{bbody} (keV)	τ	χ^2/dof[a]	Hardness[b] bbody	Flux$_{bbody}$[c]
1	2.83 ± 0.31	2.57 ± 0.45	1.18	3.36 ± 0.07	5.27 ± 0.04
2	3.82 ± 0.40	2.16 ± 0.77	1.08	4.94 ± 0.13	13.76 ± 0.10
3	2.98 ± 0.58	1.91 ± 0.85	0.96	3.07 ± 0.05	37.48 ± 0.19
4	2.21 ± 0.04	0.01 ± 0.01	0.67	0.54 ± 0.01	43.37 ± 0.21
5	2.29 ± 0.03	0.01 ± 0.01	0.66	0.60 ± 0.01	73.84 ± 0.30
6	2.47 ± 0.01	0.01 ± 0.01	1.79	0.71 ± 0.01	26.81 ± 0.17
7	2.17 ± 0.04	0.01 ± 0.01	0.72	0.54 ± 0.01	49.46 ± 0.26
8	2.18 ± 0.04	0.07 ± 0.05	0.92	0.53 ± 0.01	53.56 ± 0.28
9	2.19 ± 0.03	0.09 ± 0.08	0.74	0.52 ± 0.01	55.90 ± 0.27
10	2.28 ± 0.05	0.21 ± 0.21	0.52	0.59 ± 0.01	48.14 ± 0.27
12	2.25 ± 0.03	0.01 ± 0.01	0.60	0.59 ± 0.01	56.81 ± 0.28
19	2.21 ± 0.03	0.06 ± 0.04	0.86	0.54 ± 0.01	73.73 ± 0.28
30	2.06 ± 0.05	0.07 ± 0.03	0.75	0.51 ± 0.01	27.71 ± 0.14
40	1.83 ± 0.10	0.34 ± 0.23	0.95	0.37 ± 0.00	14.42 ± 0.07
41	1.84 ± 0.02	0.04 ± 0.02	1.09	0.37 ± 0.01	11.89 ± 0.06
42	1.67 ± 0.05	0.10 ± 0.01	0.91	0.30 ± 0.00	8.92 ± 0.04
43	1.80 ± 0.01	0.40 ± 0.03	1.35	0.45 ± 0.01	5.52 ± 0.03
44	1.64 ± 0.04	0.34 ± 0.03	1.76	0.41 ± 0.01	5.50 ± 0.03
45	3.60 ± 0.60	2.66 ± 0.60	0.91	3.67 ± 0.12	3.64 ± 0.04
46	3.17 ± 0.47	3.15 ± 0.48	1.32	3.55 ± 0.04	3.06 ± 0.02
47	2.51 ± 0.24	3.00 ± 3.00	1.07	2.89 ± 0.09	2.73 ± 0.03
48	2.70 ± 0.30	2.68 ± 0.17	1.17	3.28 ± 0.08	2.40 ± 0.02
49	2.14 ± 0.16	2.99 ± 0.05	1.24	2.54 ± 0.06	1.91 ± 0.02
50	2.39 ± 0.25	3.01 ± 0.08	0.84	2.75 ± 0.09	1.77 ± 0.02
51	3.24 ± 1.59	2.74 ± 2.61	0.56	1.82 ± 0.44	0.47 ± 0.06

Notes.
[a] The degree of freedom (dof) is 50 for all observations.
[b] Hardness parameters are obtained using the flux ratio of two different energy ranges: $F(10–30 \text{ keV})/F(3–10 \text{ keV})$.
[c] Unabsorbed fluxes of the blackbody components are in units of 10^{-10} erg s^{-1} cm^{-2}.

than predicted by the existing theoretical models for spherical accretion (Lipunov & Shakura 1976) and quasi-spherical accretion (Menou et al. 1999).

Herein, the outcome of the analysis of the X-ray data of the 2000 and 2011 outbursts allows us to better represent the emission from the hot spots on the NS as the result of accretion. By using only the blackbody light curves for these outbursts, we transform the flux versus time data to the fraction ($f \equiv \dot{M}_*/\dot{M}$) versus fastness parameter (ω_*) domain. Comparing all outbursts in this domain finds that different outbursts with different timescales and maximum fluxes follow a similar path in $f - \omega_*$. The steplike function representing the outbursts in f versus ω_* space is a function constrained in a narrow band for this system (Aql X–1). The abruptness, δ, of the step function given in Equation (8) must be related to the thickness of the inner layers of the disk (disk scale height H) in units of inner disk radius and the inclination angle between the rotation and magnetic dipole axis of the NS.

The transition to the propeller regime allows for an estimate of the magnetic field of the NS (Campana et al. 1998; Di Salvo & Burderi 2003; Asai et al. 2013; Campana et al. 2014; Mukherjee et al. 2015; King et al. 2016). Our continuous representation of the fraction of the accreting mass flux indicates that $f_c = 0.5$ (see Figure 5) when $R_{\rm in} = R_c$ ($\omega_{\rm ast} = 1$). This leads to a higher estimate of the magnetic dipole moment that is $\sqrt{2} \simeq 1.5$ times greater than the previous

estimates, which assume $f = 1$ when at this stage. We find that

$$\mu = 8.0 \times 10^{26} \text{ G cm}^3 M_{1.4}^{1/3} R_{10}^{1/2}$$
$$\left(\frac{\xi}{0.5}\right)^{-7/4} \left(\frac{L_c}{1.1 \times 10^{37} \text{ erg s}^{-1}}\right)^{1/2}, \qquad (9)$$

where $M_{1.4}$ is the mass of the NS in units of 1.4 $M_\odot$ and $R_{10} = R_*/10^6$ cm. Here we assumed $L_c = 1.1 \times 10^{37}$ erg s^{-1}, which we inferred from the "knee" seen in the light curves of the 1997 and 2010 outbursts in Figure 4.

Our assumption that the rapid-decay stage corresponds to the weak propeller regime is not commonly accepted. Given the existence of black hole systems that also show a similar knee in the light curve, it may be argued that the rapid-decay stage is a property of the disk instability model underlying the outburst (King & Ritter 1998; Campana et al. 2014). According to this picture, a cooling front moving inward in the disk is the cause of the transition to the rapid-decay stage. The possibility that the knee seen in the X-ray light curves of outbursting systems is due to the transition to the propeller stage, as well as to the disk instability, is argued in the literature (e.g., Gilfanov et al. 1998; Ibragimov & Poutanen 2009; Ekşi & Kutlu 2011; Asai et al. 2013; Güngör et al. 2014). The narrow range of δ values characterizing the transition, as we inferred in this work, supports the view that the rapid-decay stage represents the transition to the partial accretion regime. The wide range of $f_{\rm min}$

values may then indicate the varying contribution of sources other than accretion (such as cooling of the star) to the quiescence luminosity. This would imply that the rapid-decay stage in black hole systems has a different cause than that in NS systems, such as the truncation of the disk.

6. Conclusions

Based on our model and the related investigation, we conclude the following.

1. The range $\omega_* \lesssim 0.9$ is the slow-decay stage. All of the material transferred from the outer disk accretes onto the NS. As $\dot{M}$ $(=\dot{M}_*$ in the accretion stage) decreases in time, the luminosity declines (slow-decay stage), while R_{in} expands back to R_c.
2. The range $0.9 \lesssim \omega_* \lesssim 1.1$ is the partial accretion regime. A fraction of inflowing material to the inner layers of the disk may transfer onto the NS. The rest may be thrown to the outer layers of the disk or expelled from the system via a jet mechanism.
3. The range $\omega_* \gtrsim 1.1$ is the fully developed propeller stage, and the NS may even act as an isolated NS (Ekşi & Alpar 2005).

ORCID iDs

K. Y. Ekşi ⬝ https://orcid.org/0000-0001-5999-0553
E. Göğüş ⬝ https://orcid.org/0000-0002-5274-6790
T. Güver ⬝ https://orcid.org/0000-0002-3531-9842

References

Asai, K., Matsuoka, M., Mihara, T., et al. 2013, ApJ, 773, 117
Balucinska-Church, M., & McCammon, D. 1992, ApJ, 400, 699
Campana, S., Brivio, F., Degenaar, N., et al. 2014, MNRAS, 441, 1984
Campana, S., Coti Zelati, F., & D'Avanzo, P. 2013, MNRAS, 432, 1695
Campana, S., Gastaldello, F., Stella, L., et al. 2001, ApJ, 561, 924
Campana, S., Stella, L., Mereghetti, S., et al. 1998, ApJL, 499, L65
Cannizzo, J. K., Lee, H. M., & Goodman, J. 1990, ApJ, 351, 38
Casella, P., Altamirano, D., Patruno, A., Wijnands, R., & van der Klis, M. 2008, ApJL, 674, L41
Cui, W. 1997, ApJL, 482, L163
D'Angelo, C. R., & Spruit, H. C. 2010, MNRAS, 406, 1208
D'Angelo, C. R., & Spruit, H. C. 2011, MNRAS, 416, 893
Davidson, K., & Ostriker, J. P. 1973, ApJ, 179, 585
Di Salvo, T., & Burderi, L. 2003, A&A, 397, 723
Ekşi, K. Y., & Alpar, M. A. 2005, ApJ, 620, 390
Ekşi, K. Y., & Kutlu, E. 2011, in AIP Conf. Ser. 1379, Astrophysics of Neutron Stars 2010: A Conference in Honor of M. Ali Alpar, ed. E. Göğüş, T. Belloni, & Ü Ertan (Melville, NY: AIP), 156
Elsner, R. F., & Lamb, F. K. 1977, ApJ, 215, 897
Frank, J., King, A., & Raine, D. J. 2002, Accretion Power in Astrophysics (3rd ed.; Cambridge: Cambridge Univ. Press)
Galloway, D. K., Muno, M. P., Hartman, J. M., Psaltis, D., & Chakrabarty, D. 2008, ApJS, 179, 360
Ghosh, P., & Lamb, F. K. 1979a, ApJ, 232, 259
Ghosh, P., & Lamb, F. K. 1979b, ApJ, 234, 296
Gilfanov, M., Revnivtsev, M., Sunyaev, R., & Churazov, E. 1998, A&A, 338, L83
Güngör, C., Ekşi, K. Y., & Göğüş, E. 2017, NewA, 56, 1
Güngör, C., Güver, T., & Ekşi, K. Y. 2014, MNRAS, 439, 2717
Ibragimov, A., & Poutanen, J. 2009, MNRAS, 400, 492
Illarionov, A. F., & Sunyaev, R. A. 1975, A&A, 39, 185
King, A. L., Tomsick, J. A., Miller, J. M., et al. 2016, ApJL, 819, L29
King, A. R., & Ritter, H. 1998, MNRAS, 293, L42
Koyama, K., Inoue, H., Makishima, K., et al. 1981, ApJL, 247, L27
Lamb, F. K., Pethick, C. J., & Pines, D. 1973, ApJ, 184, 271
Lasota, J.-P. 2001, NewAR, 45, 449
Lin, D., Remillard, R. A., & Homan, J. 2007, ApJ, 667, 1073
Lipunov, V. M., Börner, G., & Wadhwa, R. S. 1992, Astrophysics of Neutron Stars (Berlin: Springer), 108
Lipunov, V. M., & Shakura, N. I. 1976, SvAL, 2, 133
Lipunova, G. V., & Shakura, N. I. 2002, ARep, 46, 366
Liu, B. F., Yuan, W., Meyer, F., Meyer-Hofmeister, E., & Xie, G. Z. 1999, ApJL, 527, L17
Lyubarskij, Y. E., & Shakura, N. I. 1987, SvAL, 13, 386
Maccarone, T. J., & Coppi, P. S. 2003, A&A, 399, 1151
Maitra, D., & Bailyn, C. D. 2008, ApJ, 688, 537
Menou, K., Esin, A. A., Narayan, R., et al. 1999, ApJ, 520, 276
Meshcheryakov, A. V., Tsygankov, S. S., Khamitov, I. M., et al. 2017, MNRAS, submitted (arXiv:1703.09159)
Meyer, F., Liu, B. F., & Meyer-Hofmeister, E. 2000, A&A, 361, 175
Mukherjee, D., Bult, P., van der Klis, M., & Bhattacharya, D. 2015, MNRAS, 452, 3994
Özsükan, G., Ekşi, K. Y., Hambaryan, V., et al. 2014, ApJ, 796, 46
Patruno, A., & Watts, A. L. 2012, arXiv:1206.2727
Pringle, J. E., & Rees, M. J. 1972, A&A, 21, 1
Remillard, R. A., & McClintock, J. E. 2006, ARA&A, 44, 49
Romanova, M. M., & Owocki, S. P. 2015, SSRv, 191, 339
Romanova, M. M., Ustyugova, G. V., Koldoba, A. V., & Lovelace, R. V. E. 2004, ApJL, 616, L151
Sakurai, S., Yamada, S., Torii, S., et al. 2012, PASJ, 64, 72
Shakura, N. I., & Sunyaev, R. A. 1973, A&A, 24, 337
Spruit, H. C., & Taam, R. E. 1993, ApJ, 402, 593
Suleimanov, V. F., Lipunova, G. V., & Shakura, N. I. 2008, A&A, 491, 267
Sunyaev, R. A., & Shakura, N. I. 1977, PAZh, 3, 262
Titarchuk, L. 1994, ApJ, 434, 570
Titarchuk, L., & Lyubarskij, Y. 1995, ApJ, 450, 876
Tsygankov, S. S., Mushtukov, A. A., Suleimanov, V. F., et al. 2017, A&A, submitted (arXiv:1703.04528)
Tudose, V., Fender, R. P., Linares, M., Maitra, D., & van der Klis, M. 2009, MNRAS, 400, 2111
Ustyugova, G. V., Koldoba, A. V., Romanova, M. M., & Lovelace, R. V. E. 2006, ApJ, 646, 304
Wijnands, R., & van der Klis, M. 1998, Natur, 394, 344
Zhang, S. N., Yu, W., & Zhang, W. 1998, ApJL, 494, L71